A Visibility-Domain Reconstruction Technique for Optical Interferometry Imaging

Mu-Min Chiou and Jean-Fu Kiang*

Abstract—A visibility-domain processing for optical interferometric imaging (VP-OII) method is proposed to model the visibility distribution of an image, and a phase recovery technique is proposed to acquire additional visibility data from the powerspectrum and closure-phase data. This method requires only a few tunable parameters, and can be easily extended to include more data acquired from different instruments. By simulating the reconstruction of an LkHα 101 image, the proposed method proves a few hundreds times faster and is more resilient to noise than the conventional MIRA.

1. INTRODUCTION

Optical interferometry imaging (OII) technique was used to reconstruct an image from the measured visibility, powerspectrum and phase-closure data [1], which were related to the image via a measurement equation [2]. Due to under-sampling of measurement data in the spatial-frequency domain and atmospheric noise on the measurement data, an ill-posed inverse problem was formed when applying the OII technique. A regularization term, based on a prior solution, was chosen to reduce the ambiguity of solution due to under-sampling and to make the solution less affected by the atmospheric noise. However, the reconstructed image was dependent on the regularization term and the initial guesses [3].

Various gradient-based algorithms were proposed, including BBM (building block mapping) [4], WISARD (weak-phase interferometric sample alternating reconstruction device) [5], MIRA (multi-aperture image reconstruction algorithm) [6], IRBis (image reconstruction software using the bispectrum) [7], MACIM (Monte-Carlo imaging) [8], etc. MIRA is one of the commonly used algorithms, which is based on direct optimization under a Bayesian criterion [9]. The image is related to the visibility data via a Fourier transform pair, the deviations defined in the visibility domain and the image domain are alternately minimized to converge to the final image, and some regularization terms and weighting coefficients are required.

Optical interferometric data were collected with polychromatic instruments like PIONEER [10], VEGA [11] and GRAVITY [12]. A polychromatic optical interferometric reconstruction software (PAINTER), which is a spatiospectral image reconstruction algorithm, was proposed to alternately adjust the polychromatic images and their complex differential phases [13]. In [14], an algorithm for polychromatic interferometric imaging was proposed to acquire a spatiospectral brightness distribution, assuming that the image was composed of multiple point-like sources, and some regularization terms were designed to acquire an optimal image. In [15], an OII method was presented in terms of a supersymmetric rank-1, order-3 tensor built from vectors representing the image of interest. This method was applied only to small-size images due to high dimensionality of unknowns.

Modern computer and control technology has enabled the interferometric combination of light from separate telescopes in the visible and infrared regimes [16]. Large amount of visibility data,

powerspectrum and closure-phase will be provided with optical interferometers. Taking VLTI Spectro-Imager (VSI) for example, 28 visibility data in every wavelength channel are measured within a few minutes by combining up to 8 telescopes. Assuming an observation period of 6 hours at sampling interval of 10 minutes in 32 channels, 32,256 data will be collected. By combining more interferometers worldwide, the amount of data will increase even more [16]. Hence, a more efficient algorithm is required to deal with the increasing trend of visibility data.

A visibility-domain processing for optical interferometric imaging (VP-OII) method is proposed in this work, which can keep pace with the data growth more easily. The VP-OII processes the data mainly in the visibility domain, instead of switching between the image and the visibility domains. This method depends less on the initial guesses, and the number of tunable parameters are very limited.

An image of LkHα 101 [17] is adopted for testing in this work, and the optical interferometric data are simulated on the configuration of the six-station Navy Prototype Optical Interferometer (NPOI) [18] plus GRAVITY to verify the efficacy of the proposed method. If the brightness distribution has a weak dependence on wavelengths [9, 19], polychromatic measurement data can be used to further enhance the reconstructed image [14, 20]. Based on this idea, the powerspectrum and phase-closure data at multiple wavelengths are simulated on the configurations of NPOI and CHARA [11], to acquire additional visibility data.

This paper is organized as follows. The MIRA is briefly reviewed in Section 2; the proposed VP-OII method is presented in Section 3; the simulation scenario and results are discussed in Sections 4. Finally, some conclusions are drawn in Section 5.

2. REVIEW OF MULTI-APERTURE IMAGE RECONSTRUCTION ALGORITHM (MIRA)

A visibility data $v_{pq} = |v_{pq}|e^{j\phi_{pq}}$ is derived from the measurement data of two telescopes, T_p and T_q. The phase difference measured between T_p and T_q is degraded by the atmospheric turbulence as [9]

$$\phi_{pq}^{\text{mea}} = \phi_{pq} + \psi_q - \psi_p + n_{pq} \tag{1}$$

where $\psi_q - \psi_p$ is the differential piston induced by turbulence, and n_{pq} is an additive noise. Given a set of three telescopes, T_p, T_q and T_r, three phase data can be represented as

$$\phi_{pq}^{\text{mea}} = \phi_{pq} + \psi_q - \psi_p + n_{pq}, \qquad \phi_{qr}^{\text{mea}} = \phi_{qr} + \psi_r - \psi_q + n_{qr}, \qquad \phi_{rp}^{\text{mea}} = \phi_{rp} + \psi_p - \psi_r + n_{rp}$$

along with a phase-closure data

$$\beta_{pqr}^{\text{mea}} = \text{mod}\left\{\phi_{pq}^{\text{mea}} + \phi_{qr}^{\text{mea}} + \phi_{rp}^{\text{mea}}, 2\pi\right\} = \text{mod}\left\{\phi_{pq} + \phi_{qr} + \phi_{rp} + n_{pqr}, 2\pi\right\} \tag{2}$$

where $n_{pqr} = n_{pq} + n_{qr} + n_{rp}$, and the differential pistons are canceled out.

Any phase-closure data β_{pqr} can be represented in terms of three phase-closure data that involving telescope T_1 as $\beta_{pqr} = \beta_{1pq} + \beta_{1qr} + \beta_{1rp}$. Thus, there will be $(N_t-1)(N_t-2)/2$ independent phase-closure data when N_t telescopes are used [9]. A powerspectrum data is related to a visibility data as

$$s_{pq}^{\text{mea}} = |v_{pq}|^2 + n_{s_{pq}} \tag{3}$$

where $n_{s_{pq}}$ is a zero-mean Gaussian noise, with its variance depending on the integration time.

Figure 1 shows the coordinate systems to present the image, the visibility data and the telescope positions; where $\hat{\nu}_u$ and $\hat{\nu}_v$ are the unit vectors parallel to the geographic east-west and north-south directions, respectively; $\hat{\theta}_u$ and $\hat{\theta}_v$ are the unit vectors parallel to $\hat{\nu}_u$ and $\hat{\nu}_v$, respectively; (θ_u, θ_v) is the angular position of an image pixel, measured with respect to the image center at $\bar{r}_c$; (ν_u, ν_v) represents a baseline in unit of wavelengths; $\bar{r}_p$ and $\bar{r}_q$ are the position vectors of telescopes T_p and T_q, respectively.

The visibility data v_{n_v}, of an image $\bar{x}$, at the spatial frequency $\bar{\nu}_{n_v}$ is represented as [3]

$$v_{n_v} = \sum_{n=1}^{N} e^{j2\pi\bar{\theta}_n \cdot \bar{\nu}_{n_v}} x_n \tag{4}$$

with $1 \le n_v \le N_v$, where N and N_v are the number of image pixels and visibility data, respectively. The nth image pixel is located at $\bar{\theta}_n = \hat{\theta}_u \theta_{un} + \hat{\theta}_v \theta_{vn}$, and the n_vth visibility data is located at $\bar{\nu}_{n_v} = \hat{\nu}_u \nu_{un_v} + \hat{\nu}_v \nu_{vn_v}$.
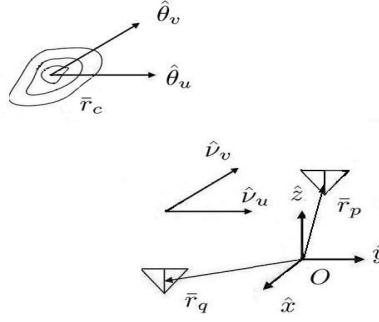
Figure 1. Coordinate systems to present image and visibility data, the telescopes are labeled with the Earth-centered Earth-fixed coordinates.

The image can be reconstructed from the measurement data and the prior information, by minimizing an object function as [6]

$$\bar{x}_{\text{opt}} = \arg \min_{\bar{x} \in \Omega} \left\{ f_{\bar{x}}(\bar{x}, \bar{v}^{\text{mea}}, \bar{s}^{\text{mea}}, \bar{\beta}^{\text{mea}}) + c_1 f_{\text{prior}}(\bar{x}, \bar{x}^{\text{prior}}) \right\} \tag{5}$$

where $\bar{v}^{\text{mea}}$, $\bar{s}^{\text{mea}}$ and $\bar{\beta}^{\text{mea}}$ are the measured visibility, powerspectrum and phase-closure data, respectively; $f_{\text{prior}}(\bar{x})$ is a regularization function, c_1 is a hyper-parameter, and

$$\Omega = \left\{ \bar{x} \mid x_n \geq 0, \sum_{n=1}^{N} x_n = 1 \right\} \tag{6}$$

is a set of normalized images with non-negative pixels.

A modeled visibility of an image $\bar{x}$ is computed as

$$\bar{v}^{\text{mod}} = \bar{\bar{H}} \cdot \bar{x} \tag{7}$$

where $\bar{\bar{H}}$ is a transform matrix corresponding to a nonuniform discrete Fourier transform. In Eq. (5), $f_{\bar{x}}(\bar{x}, \bar{v}^{\text{mea}}, \bar{s}^{\text{mea}}, \bar{\beta}^{\text{mea}})$ characterizes the difference between the modeled and the measured data, which can be further decomposed into

$$f_{\bar{x}}(\bar{x}, \bar{v}^{\text{mea}}, \bar{s}^{\text{mea}}, \bar{\beta}^{\text{mea}}) = f_{xv}(\bar{x}, \bar{v}^{\text{mea}}) + f_{xp}(\bar{x}, \bar{s}^{\text{mea}}) + f_{xc}(\bar{x}, \bar{\beta}^{\text{mea}}) \tag{8}$$

with

$$f_{xv}(\bar{x}, \bar{v}^{\text{mea}}) = \sum_{p<q} \frac{\left| v_{pq}^{\text{mod}} - v_{pq}^{\text{mea}} \right|^2}{\text{var}\left\{ v_{pq}^{\text{mea}} \right\}}, \quad f_{xp}(\bar{x}, \bar{s}^{\text{mea}}) = \sum_{p<q} \frac{\left[s_{pq}^{\text{mea}} - s_{pq}^{\text{mod}} \right]^2}{\text{var}\left\{ s_{pq}^{\text{mea}} \right\}},$$

$$f_{xc}(\bar{x}, \bar{\beta}^{\text{mea}}) = \sum_{p<q<r} \frac{\left| e^{j\beta_{pqr}^{\text{mea}}} - e^{j\beta_{pqr}^{\text{mod}}} \right|^2}{\text{var}\left\{ \beta_{pqr}^{\text{mea}} \right\}} \tag{9}$$

The function in Eq. (8) is non-convex [3], hence the reconstructed image could be sensitive to the prior information and the initial guess.

In this work, we choose a prior function, commonly used in MIRA, as [3]

$$f_{\text{prior}}(\bar{x}, \bar{x}^{\text{prior}}) = \sum_{n=1}^{N} \frac{x_n^2}{x_n^{\text{prior}}} \tag{10}$$

and a Lorentzian model, proper for characterizing a compact object [2], is applied to generate $\bar{x}^{\text{prior}}$ as [9]

$$x_n^{\text{prior}} \propto \frac{1}{1 + 2(\theta_u^2 + \theta_v^2)/(\Delta\theta_w)^2} \tag{11}$$
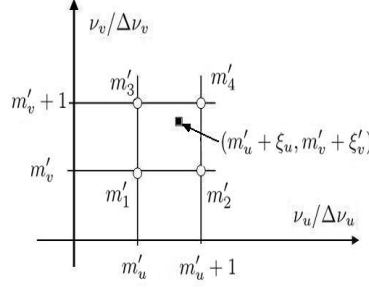
Figure 2. Interpolating visibility data at $\bar{\nu}_{n'} = (\nu'_u, \nu'_v)$ by using four surrounding visibility data, $v[m'_1]$, $v[m'_2]$, $v[m'_3]$ and $v[m'_4]$, defined on a rectangular grid.

where $\Delta\theta_w$ is the angular span of the image. To avoid being trapped in a local minimum, the MIRA begins with a large c_1, putting more weight on the prior information. As the iteration moves on, c_1 is gradually decreased [9], and the convergent solution is claimed when c_1 drops below a given threshold. In this work, c_1 is set to 10 in the beginning, and is reduced by half each time, until it drops to 10×2^{-7}. At each c_1, as many as 70 iterations are allowed.

3. PROPOSED VP-OII METHOD

Figure 2 shows a rectangular grid in the visibility plane, with cell size of $\Delta\nu_u \times \Delta\nu_v$. The visibility data on the grid, $v[m_u, m_v] = v(m_u\Delta\nu_u, m_v\Delta\nu_v)$, are stored in a vector $v[m]$. Each modeled visibility data corresponding to a given measurement data is interpolated from four surrounding visibility data on the rectangular grid via a bilinear interpolation as

$$v_{n'}^{\text{mod}} = \sum_{i=1}^{4} R_{n',m'_i} v[m'_i] \tag{12}$$

where all elements in the n'th row of matrix $\bar{\bar{R}}$ are reset to zero, except

$$R_{n',m'_1} = (1 - \xi'_v)(1 - \xi'_u), \qquad R_{n',m'_2} = \xi'_u(1 - \xi'_v), \qquad R_{n',m'_3} = \xi'_u\xi'_v, \qquad R_{n',m'_4} = \xi'_v(1 - \xi'_u)$$

m'_1, m'_2, m'_3 and m'_4 are the one-dimensional indices of (m'_u, m'_v), $(m'_u + 1, m'_v)$, $(m'_u + 1, m'_v + 1)$ and $(m'_u, m'_v + 1)$, respectively, with

$$m'_u = \left\lfloor \frac{\nu'_u}{\Delta\nu_u} \right\rfloor, \qquad m'_v = \left\lfloor \frac{\nu'_v}{\Delta\nu_v} \right\rfloor, \qquad \xi'_u = \frac{\nu'_u - m'_u\Delta\nu_u}{\Delta\nu_u}, \qquad \xi'_v = \frac{\nu'_v - m'_v\Delta\nu_v}{\Delta\nu_v}$$

Instead of computing the visibility data via a Fourier transform on the image data as in (4), the modeled visibility data in (12) are acquired in a more efficient way.

3.1. Phase Recovery Technique

Figure 3 shows the schematic of phase recovery, in which the phase of additional visibility data is derived by using the phase-closure data. The shaded area in the visibility plane contains the visibility data with known phase, which are derived from a low-resolution image or simulated with the GRAVITY configuration.

A measured phase-closure β_{pqr}^{mea} is the sum of ϕ_{pq}, ϕ_{qr} and ϕ_{rp}, which are derived from the data of telescopes T_p, T_q and T_r, respectively. Thus, if ϕ_{pq} and ϕ_{qr} are known, ϕ_{rp} can be derived as

$$\phi_{rp} = \beta_{pqr}^{\text{mea}} - \phi_{pq} - \phi_{qr} \tag{13}$$

Similarly, Eq. (3) can be used to derive the amplitude of visibility data ($|v_{rp}|$), associated with ϕ_{rp}, from the powerspectrum data. As a result, additional visibility data are acquired to expand the shaded region in Fig. 3. The variance of the recovered visibility v_{rp} is estimated as

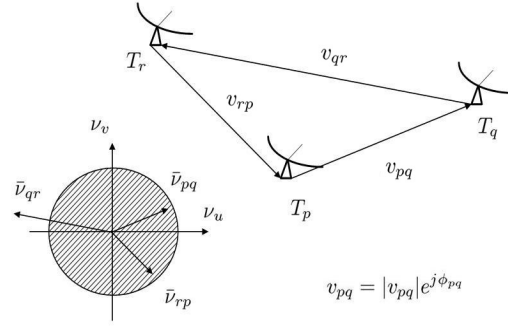$$\text{var}\{v_{rp}\} = \sqrt{\text{var}\{v_{pq}\}\text{var}\{v_{qr}\}}$$

Figure 3. Schematic of phase recovery.

The phase recovery technique is applied in an iterative manner. In the beginning, the available visibility data contain only the measured visibility data, namely, $\bar{v}^{\mathrm{ava}(0)} = \bar{v}^{\mathrm{mea}}$. In the ℓth iteration, the available visibility data are expanded to $\bar{v}^{\mathrm{ava}(\ell)}$, and $\bar{v}^{\mathrm{rec}(\ell)}$ contains the recovered visibility data. The shaded area in Fig. 3 is expanded to $\bar{v}^{\mathrm{ava}(\ell+1)}$ as

$$\bar{v}^{\mathrm{ava}(\ell+1)} = \bar{v}^{\mathrm{ava}(\ell)} \oplus \bar{v}^{\mathrm{rec}(\ell)}$$

where $\oplus$ is a concatenation operator. When no more visibility data can be recovered in the Lth iteration, the total available data will become $\bar{v}^{\mathrm{ava}(L)}$.

3.2. Initial Guess

The initial guess of visibility data is obtained by applying the BFGS algorithm [6] to optimize an object function as

$$\bar{v}_0^{(\ell+1)} = \arg \ \min_{\bar{v} \in \Omega_b} \left\{ f_{vv}(\bar{v}, \bar{v}^{\mathrm{ava}(\ell)}) \right\}, \qquad \ell = 0, 1, \ldots \tag{14}$$

where $\Omega_b = \{\bar{v} | \bar{v} = 1 \text{ at } \bar{\nu} = 0\}$,

$$f_{vv}(\bar{v}, \bar{v}^{\mathrm{ava}(\ell)}) = \sum_{n_v=1}^{N_v + N_v^{\mathrm{rec}(\ell)}} w_{n_v}^v \left| v_{n_v}^{\mathrm{mod}} - v_{n_v}^{\mathrm{ava}(\ell)} \right|^2 \tag{15}$$

$w_{n_v}^v = 1/\mathrm{var} \left\{ v_{pq}^{\mathrm{mea}} \right\}$ is a weighting coefficient, which is the same as that in Eq. (9); N_v and $N_v^{\mathrm{rec}(\ell)}$ are the numbers of visibility data in $\bar{v}^{\mathrm{ava}(0)}$ and $\bar{v}^{\mathrm{rec}(\ell)}$, respectively.

In this work, the first initial guess $(\bar{v}^{\mathrm{mea}(0)})$ is derived from the simulated data on the GRAVITY configuration, labeled as $\bar{v}_{\mathrm{G}}^{\mathrm{mea}(0)}$. The iteration process in Eq. (14) is continued until no more visibility data can be recovered, and the results of the last iteration will be used as the optimal initial guess, labeled as $\bar{v}_0^{\mathrm{opt}}$.

3.3. Optimal Solution

The optimal solution is obtained by minimizing an object function defined as

$$\bar{v}^{\mathrm{opt}} = \arg \ \min_{\bar{v} \in \Omega_b} \left\{ f_{vv}(\bar{v}, \bar{v}^{\mathrm{mea}(0)}) + f_{vp}(\bar{v}, \bar{s}^{\mathrm{mea}}) + f_{vc}(\bar{v}, \bar{\beta}^{\mathrm{mea}}) \right\} \tag{16}$$

where

$$f_{vp}(\bar{v}, \bar{s}^{\mathrm{mea}}) = \sum_{n_p=1}^{N_p} w_{n_p}^p (s_{n_p}^{\mathrm{mod}} - s_{n_p}^{\mathrm{mea}})^2, \qquad f_{vc}(\bar{v}, \bar{\beta}^{\mathrm{mea}}) = \sum_{n_c=1}^{N_c} w_{n_c}^c \left| e^{j\beta_{n_c}^{\mathrm{mea}}} - e^{j\beta_{n_c}^{\mathrm{mod}}} \right|^2$$

are the object functions related to powerspectrum and phase-closure, respectively; N_p and N_c are the numbers of powerspectrum and phase-closure data, respectively; $w_{n_p}^p$'s and $w_{n_c}^c$'s are weighting coefficients [3], which are set to $w_{n_p}^p = \mathrm{var}\{s_{n_p}^{\mathrm{mea}}\}$ and $w_{n_c}^c = \mathrm{var}\{\beta_{n_c}^{\mathrm{mea}}\}$, as in the conventional MIRA [6]. The modeled powerspectrum $s_{n_p}^{\mathrm{mod}}$ and phase-closure $\beta_{n_c}^{\mathrm{mod}}$ are computed as

$$s_{n_p}^{\mathrm{mod}} = \left| v_{n_p}^{\mathrm{mod}} \right|^2, \qquad \beta_{n_c}^{\mathrm{mod}} = \sum_{k=1}^{3} \phi_{k,n_c}^{\mathrm{mod}}$$

where $\phi_{k,n_c}^{\mathrm{mod}}$ is the kth phase component of the n_cth phase-closure measurement.

The BFGS algorithm is then applied to solve Eq. (16) to obtain the convergent visibility distribution $\bar{v}^{\mathrm{opt}}$, with $\bar{v}_0^{\mathrm{opt}}$ as the initial guess. The final image is then acquired by taking the two-dimensional inverse Fourier transform of $\bar{v}^{\mathrm{opt}}$ as

$$\bar{x} = \bar{\bar{F}}^{-1} \cdot \bar{v}^{\mathrm{opt}} \tag{17}$$

At last, each image pixel is adjusted to have non-negative value as

$$x_n = \begin{cases} x_n, & x_n \geq 0 \\ \\ 0, & x_n < 0 \end{cases}$$

The only empirical parameters needed in the VP-OII algorithm are the grid intervals $\Delta\nu_u$ and $\Delta\nu_v$. When applying the phase recovery technique to exploit more information embedded in the closure-phase data, potential error may be induced to the recovered visibility data. A more cautious approach is taken by using these recovered data to obtain an optimal initial guess $\bar{v}_0^{\mathrm{opt}}$, while $\bar{v}^{\mathrm{mea}(0)}$ is used to find the optimal solution $\bar{v}^{\mathrm{opt}}$ by solving Eq. (16).

4. SIMULATIONS AND DISCUSSIONS

Figure 4 shows an image of LkHα 101 observed at wavelength of 550 nm, which covers 12 milli-arcsecond (mas) along both axes. The LkHα 101 has the diameter of about 5.5 mas [17], and is located at the right ascension of $4^{\mathrm{h}}30^{\mathrm{m}}14.4^{\mathrm{s}}$, the declination of $35°16'24''$, and at a distance of 700 parsec (pc) from the Earth [17]. This image will be used as the reference image $\bar{x}^{\mathrm{ref}}$ for simulations, which is composed of 256×256 pixels, with an angular resolution of 0.0469 mas/pixel.

Figure 5 shows the real part of the visibility data $\bar{v}^{\mathrm{ref}}$, which is the Fourier transform of $\bar{x}^{\mathrm{ref}}$ shown in Fig. 4. The grid intervals are $\Delta\nu_{u,\mathrm{def}} = 1/(N_g\Delta\theta_u)$ and $\Delta\nu_{v,\mathrm{def}} = 1/(N_g\Delta\theta_v)$, equivalent to $1.722 \times 10^7\lambda$ if $N_g = 256$.
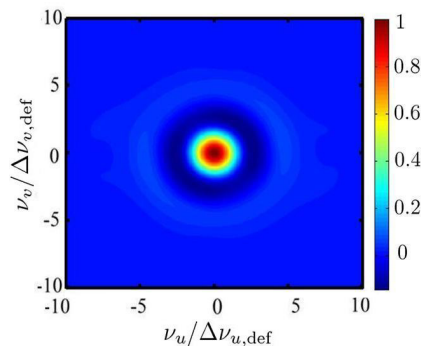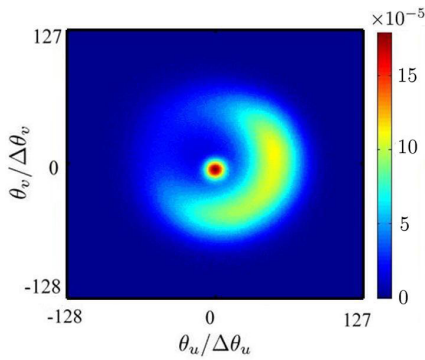

Figure 4. Image of LkHα 101 at $\lambda = 550$ nm [17].

Figure 5. Real part of reference visibility data, $\mathrm{Re}\{\bar{v}^{\mathrm{ref}}\}$, with $\Delta\nu_{u,\mathrm{def}} = \Delta\nu_{v,\mathrm{def}} = 1.722 \times 10^7\lambda$ and $N_g = 256$.

4.1. Initial Guess

Figure 6(a) shows the visibility data simulated with the GRAVITY configuration, which is centered at $(70.40479659°\,\mathrm{W}, 24.6279483°\,\mathrm{S})$, by artificially setting the declination of LkHα 101 to $-35°16'24"$, making it observable to the GRAVITY configuration. The polychromatic data set are simulated with the configurations of optical interferometric telescopes, NPOI, CHARA and GRAVITY. The geometrical positions of telescopes, wavelengths and acquisition time are generated by using the ASPRO2 software.

The grid intervals are set to $\Delta\nu_u = \Delta\nu_{u,\mathrm{def}}/2$ and $\Delta\nu_v = \Delta\nu_{v,\mathrm{def}}/2$, which satisfy the general requirement that $\Delta\nu_{u,\mathrm{def}}/4 \leq \Delta\nu_u \leq \Delta\nu_{u,\mathrm{def}}$. Smaller grid intervals are preferred to update the initial guess in Eq. (14) if the visibility changes significantly over the grid. However, choosing small grid intervals may result in too many grid cells void of visibility data.

The initial guess will be optimized by using the visibility data shown in Fig. 6(a) as well as the phase-closure data $\bar{\beta}^{\mathrm{mea}}$ and the powerspectrum data $\bar{s}^{\mathrm{mea}}$ simulated with the NPOI configuration. As was mentioned, the GRAVITY configuration is capable of measuring the visibility data with phase, while the NPOI can only measure the powerspectrum and the closure-phase data. Fig. 6(b) shows the real part of the first initial guess $\mathrm{Re}\{\bar{v}_0^{(1)}\}$, which contains mostly the measured visibility data.

Figure 7(a) shows the powerspectrum data $(\bar{s}^{\mathrm{mea}})$ simulated with the NPOI configuration. By iteratively applying the phase recovery technique, additional visibility data are recovered as shown in Fig. 7(b).
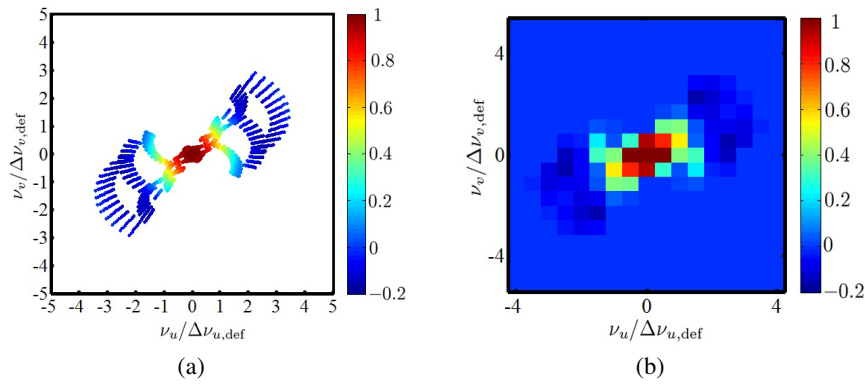

Figure 6. (a) Real part of visibility data, $\mathrm{Re}\{\bar{v}_{\mathrm{G}}^{\mathrm{mea}(0)}\}$, simulated with GRAVITY configuration over wavelengths of 1.97272–2.42727 µm, in 11 channels [12]. (b) Real part of first initial guess, $\mathrm{Re}\{\bar{v}_0^{(1)}\}$.
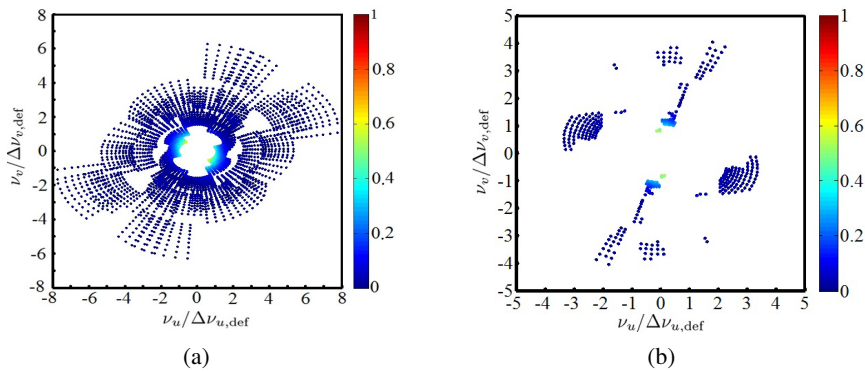

Figure 7. (a) Powerspectrum data $(\bar{s}^{\mathrm{mea}})$ simulated with NPOI configuration over wavelengths of 0.58177–0.84822 µm, in 9 channels. (b) Real part of additional visibility data acquired with phase recovery technique.

4.2. Accuracy of Modeled Phases

The phase error in applying the phase recovery technique is estimated by defining a deviation

$$\varepsilon = \sqrt{\frac{1}{N_v^{\text{rec}}} \sum_{n_v=1}^{N_v^{\text{rec}}} \left(\phi_{n_v}^{\text{rec}} - \phi_{n_v}^{\text{mea}}\right)^2}$$

where $\phi_{n_v}^{\text{rec}}$ and $\phi_{n_v}^{\text{mea}}$ are the recovered phase and the corresponding reference phase, respectively; and N_v^{rec} is the number of recovered visibility data. In this case, $N_v^{\text{rec}} = 336$ (about 12.8%) additional visibility data are acquired from 2,640 powerspectrum data, leading to $\varepsilon = 1.37°$.

4.3. Reconstructed Visibility and Image

Figure 8(a) shows the real part of the optimal initial guess, $\text{Re}\left\{\bar{v}_0^{\text{opt}}\right\}$; and Fig. 8(b) shows the real part of the final visibility distribution, $\bar{v}^{\text{opt}}$, by solving Eq. (16). Both $\bar{v}_0^{\text{opt}}$ and $\bar{v}^{\text{opt}}$ contain more visibility data than the original distribution shown in Fig. 6(b). The available visibility data shown in Fig. 6(b) appear in the range of $-3 \leq \nu/\Delta\nu_{v,\text{def}} \leq 3$ and $-4 \leq \nu_u/\Delta\nu_{u,\text{def}} \leq 4$. As a comparison, the available visibility data in both $\bar{v}_0^{\text{opt}}$ and $\bar{v}^{\text{opt}}$ have been extended to the range of $-6 \leq \nu/\Delta\nu_{v,\text{def}} \leq 6$ and $-7 \leq \nu_u/\Delta\nu_{u,\text{def}} \leq 7$, as shown in Figs. 8(a) and 8(b), respectively. The quality of the reconstructed image is evaluated by defining a root-mean-square (rms) pixel-wise difference as [21]

$$\delta = 10^6 \times \sqrt{\sum_{n=1}^{N} x^{\text{ref}} \left(x_n - x_n^{\text{ref}}\right)^2} \text{ ppm} \tag{18}$$

In this work, we do not translate the reconstructed image before comparing it to the reference image.

Figures 9(a) and 9(b) show the reconstructed images by using VP-OII and MIRA, respectively. Table 1 lists the rms pixel-wise difference at different stages in three simulation scenarios. In the first scenario, the phase recovery technique is applied to the GRAVITY simulated data. With VP-OII, the rms pixel-wise difference of the first initial guess is 34.37 ppm, and those of the optimal initial guess and the final result are 18.90 and 15.99 ppm, respectively. The optimization of initial guess via Eq. (14) reduces most of the rms pixel-wise difference, and the optimization procedure via Eq. (16) improves further.

In the second scenario, the interferometric data from CHARA over wavelengths of 1.47493–1.75256 µm in 8 channels are included to demonstrate the efficiency of the proposed algorithm when more data become available. In the third scenario, MIRA is applied under the same condition as that in the first scenario (both NPOI and GRAVITY simulated data are used). The rms pixel-wise difference is 17.26 ppm, which is larger than that of the proposed VP-OII (15.99 ppm).

Figure 9(c) shows the reconstructed image by using the simulated data on NPOI, GRAVITY and CHARA configurations. As listed in the second scenario of Table 1, the rms pixel-wise difference
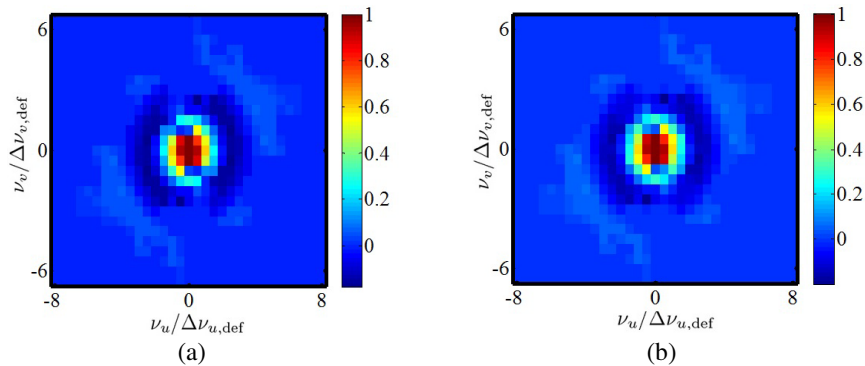

Figure 8. (a) Real part of optimal initial guess, $\text{Re}\{\bar{v}_0^{\text{opt}}\}$. (b) Real part of final visibility data, $\text{Re}\left\{\bar{v}^{\text{opt}}\right\}$.
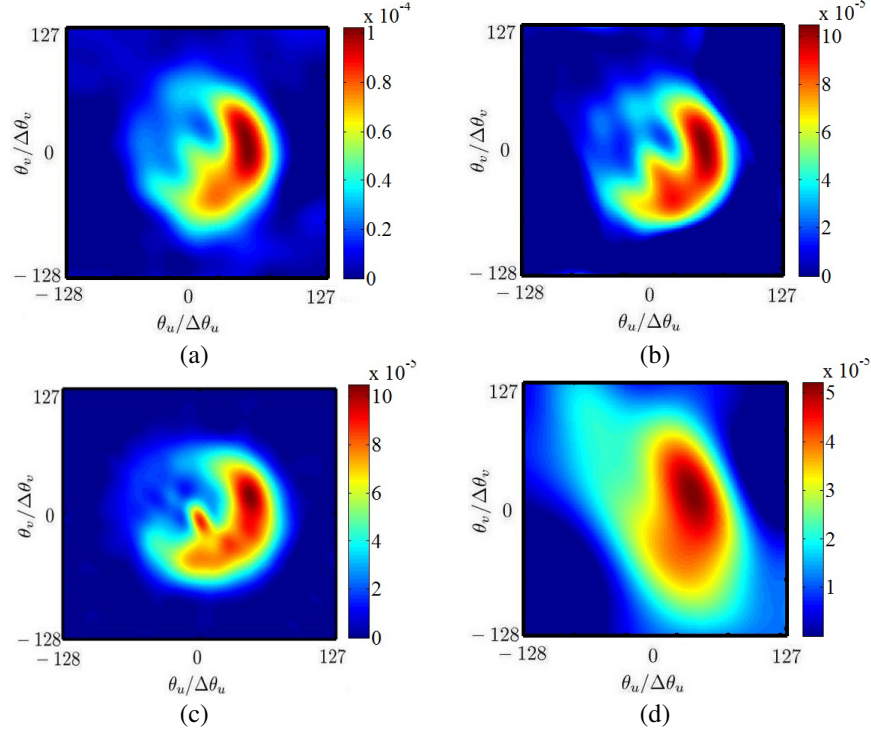
Figure 9. Reconstructed image by using (a) VP-OII and (b) MIRA. (c) Reconstructed image by using simulated data on NPOI, GRAVITY and CHARA configurations. (d) Reconstructed image by solving (16) with the original visibility data, without resorting to the phase recovery technique.

Table 1. RMS pixel-wise difference at different stages of visibility reconstruction.

method	VP-OII		MIRA
scenario	1	2	3
configuration	GRAVITY, NPOI	GRAVITY, NPOI, CHARA	GRAVITY, NPOI
$\bar{v}^{\mathrm{mea}(0)}$	$\bar{v}_{\mathrm{G}}^{\mathrm{mea}(0)}$	$\bar{v}_{\mathrm{G}}^{\mathrm{mea}(0)}$	$\bar{v}_{\mathrm{G}}^{\mathrm{mea}(0)}$
$\delta(\bar{v}_0^{(1)})$ (ppm)	34.37	32.47	
$\delta(\bar{v}_0^{\mathrm{opt}})$ (ppm)	18.90	17.87	
$\delta(\bar{v}^{\mathrm{opt}})$ (ppm)	15.99	15.15	17.26
N_v	2,640	2,640	2,640
N_v^{ret}	336	668	
N_p	3,456	4,084	3,456
N_c	2,484	7,152	2,484

is further reduced to 18.04 ppm. By including the data from the CHARA instrument, not only the number of powerspectrum and closure-phase data are increased, the number of recovered phase data is also increased. Specifically, the number of recovered phase data is increased from 336 to 668, that of powerspectrum data from 3,456 to 7,152, and that of closure-phase data from 2,484 to 4,084.

4.4. Effects of Phase Recovery Technique

Figure 10 shows the reconstructed image by using the MIRA method, with only the GRAVITY instrument data. The rms pixel-wise differences are 34.37 and 33.57 ppm by using VP-OII and MIRA,
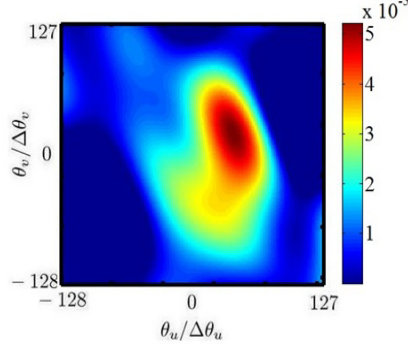
Figure 10. Reconstructed image by using MIRA method, with only GRAVITY instrument data.

respectively, based on the available *uv*-coverage shown in Fig. 6(a). The image reconstructed with MIRA (in Fig. 10) appears more compact than that with VP-OII, shown in Fig. 9(d). Because the VP-OII applies the inverse Fourier transform only after the modeled visibility data have converged, while the MIRA refines the image model to match the data in the visibility domain at each iteration. It appears that the MIRA performs better when the amount of visibility data is small.

By taking a closer look at Fig. 6(a), more visibility data are available in the directions around 1, 2, 7 and 8 o'clock, providing more information at higher spatial frequencies in these directions, hence the reconstructed image in these directions becomes clearer and more compact. On the other hand, less high spatial-frequency visibility data are available in the directions around 11 to 12 o'clock, making the reconstructed image look blurred and extended in these direction.

4.5. Computational Efficiency

Table 2 lists the numbers of multiplication/division (M/D) operations required to implement MIRA and VP-OII, respectively; where M is the total number of visibility data in the visibility-domain grid; T_{PR} is the number of iterations taken in the phase recovery process, T_{LS} is the number of iterations taken in the line search method of the BFGS algorithm, T_{MIRA} is the number of iterations taken in MIRA, T_{OB} is the number of iterations taken in updating the object function in (16); and B_i is the number of surrounding grid points used for interpolation. In the simulations, we choose $N_v = 2,640$, $N_p = 3456$, $N_c = 2484$, $N = 256^2$, $M = 5,000$, $T_{\mathrm{PR}} = 200$, $T_{\mathrm{LS}} = 10$, $T_{\mathrm{MIRA}} = 200$, $T_{\mathrm{OB}} = 200$ and $B_i = 4$. With these parameters, the numbers of M/D operations required to implement MIRA and VP-OII are 1.12×10^{11} and 4.89×10^8, respectively. The ratio of M/D operations is 230 : 1 in this case, and will become larger if the number of visibility data or the image size is increased.

Figure 9(d) shows a reconstructed image obtained by solving Eq. (16) directly, without resorting

Table 2. Number of multiplication/division operations.

MIRA [6]		VP-OII	
process	M/D	process	M/D
$\nabla_{\bar{x}} f_v$	$N_v N$ (per iteration)	phase recovery	$2T_{\mathrm{PR}} \times [3B_i N_v + T_{\mathrm{LS}}(B_i + 2)N_v]$
$\nabla_{\bar{x}} f_p$	$N_p \times N$ (per iteration)	$\nabla_{\bar{v}} f_v + \nabla_{\bar{v}} f_p + \nabla_{\bar{v}} f_c$	$6B_i(N_v + N_p + N_c)$ (per iteration)
$\nabla_{\bar{x}} f_c$	$N_c \times 3N$ (per iteration)	line search	$T_{\mathrm{LS}}(B_i + 2)(N_v + N_p + N_c)$ (per iteration)
line search	$T_{\mathrm{LS}}(N_v + N_p + 3N_c)$ (per iteration)	$\bar{\bar{F}}^{-1}$	$M \times N$
total	$T_{\mathrm{MIRA}}[(N_v + N_p + 3N_c)N + T_{\mathrm{LS}}(N_v + N_p + 3N_c)]$	total	$M \times N + [T_{\mathrm{PR}} N_v + T_{\mathrm{OB}}(N_v + N_p + N_c)] \times [3B_i + T_{\mathrm{LS}}(B_i + 2)]$

to the phase recovery technique. The image looks poorer, which implies that the initial guess is critical to the VP-OII method, and the phase recovery technique is capable of supplying additional visibility data to improve the initial guess and make VP-OII work properly.

By replacing $\bar{v}^{\mathrm{mea}(0)}$ with $\bar{v}^{\mathrm{ava}(L)}$ in Eq. (16), the rms pixel-wise differences with the initial guesses of $\bar{v}^{\mathrm{mea}(0)}$ and $\bar{v}^{\mathrm{ava}(L)}$ are 15.99 and 15.84 ppm, respectively, with NPOI/GRAVITY configurations (first scenario in Table 1). The values of δ are 15.15 and 15.64 ppm by using $\bar{v}^{\mathrm{mea}(0)}$ and $\bar{v}^{\mathrm{ava}(L)}$, respectively, as the initial guess, with NPOI/GRAVITY/CHARA configurations (second scenario in Table 1). Although $\bar{v}^{\mathrm{ava}(L)}$ contains additional visibility data acquired with the phase recovery technique, it is also contaminated by phase errors as the shaded area shown in Fig. 3 is expanded.

Table 3 lists the iteration number and CPU time taken by the MIRAs (exact and nfft) [6] and the VP-OII method, respectively. The iteration numbers of both methods are close. The CPU time of the nfft option is shorter than that of the exact option in MIRA. Yet the VP-OII algorithm takes much shorter CPU time.

Table 3. Iteration number and CPU time of MIRA and VP-OII.

	MIRA (exact)	MIRA (nfft)	VP-OII
iteration number	583	597	512
CPU time (second)	8,953	6,872	145

nfft: non-equispaced fast Fourier transform.

4.6. Effects of Noise

To study the effects of noise, a signal-to-noise ratio (SNR) is defined as [2]

$$\mathrm{SNR} = 20 \log_{10} \frac{\|\bar{v}^{\mathrm{ref}}\|_2}{\|\bar{v}^{\mathrm{mea}} - \bar{v}^{\mathrm{ref}}\|_2} \ \mathrm{dB} \tag{19}$$

Each visibility data is perturbed by noise as [22]

$$\left| v_{n_v}^{\mathrm{mea}} \right| = \left| v_{n_v}^{\mathrm{ref}} \right| + \Delta v_{a,n_v}, \qquad \phi_{n_v}^{\mathrm{mea}} = \arg \left\{ v_{n_v}^{\mathrm{ref}} \right\} + \Delta \phi_{n_v}$$

where $\Delta v_{a,n_v}$ and $\Delta \phi_{n_v}$ are independent zero-mean Gaussian noise additive to amplitude and phase, respectively, with the magnitudes related as

$$\mathrm{var}\{\Delta v_a\} = |v^{\mathrm{ref}}| \mathrm{var}\{\Delta \phi\}$$

Figures 11(a) and 11(b) show the average and the standard deviation of δ, which are obtained over 100 realizations of simulated visibility data with NPOI, GRAVITY and CHARA configurations. The standard deviation of δ is defined as

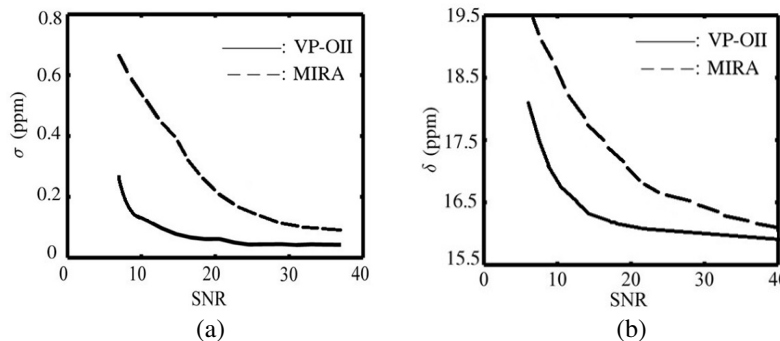$$\sigma = \sqrt{\frac{1}{N_r} \sum_{n_r=1}^{N_r} (\delta_{n_r} - \langle \delta \rangle)^2} \ \mathrm{ppm}$$

Figure 11. Effects of SNR on (a) average rms pixel-wise difference (δ) and (b) standard deviation of δ, over 100 realizations. ———: VP-OII, $- - -$: MIRA.

Table 4. Performance with different channel numbers.

	ch. no. of GRAVITY: 16, ch. no. of NPOI: 16	ch. no. of GRAVITY: 11, ch. no. of NPOI: 9	ch. no. of GRAVITY: 8, ch. no. of NPOI: 7
	$\Delta\lambda_\mathrm{G} = 0.0303\,\mu\mathrm{m}$, $\Delta\lambda_\mathrm{N} = 0.0178\,\mu\mathrm{m}$	$\Delta\lambda_\mathrm{G} = 0.045\,\mu\mathrm{m}$, $\Delta\lambda_\mathrm{N} = 0.0333\,\mu\mathrm{m}$	$\Delta\lambda_\mathrm{G} = 0.0758\,\mu\mathrm{m}$, $\Delta\lambda_\mathrm{N} = 0.0444\,\mu\mathrm{m}$
N_rec	1,120	668	474
ϵ of VP-OII	1.46	1.39	1.41
δ of VP-OII	15.13	15.15	16.03
δ of MIRA	17.17	17.26	17.41

where $\langle\delta\rangle$ is the average of δ over N_r realizations.

The rms pixel-wise difference of VP-OII is lower than that of MIRA at low SNR values, and approaches the same level at high SNR values. The VP-OII optimizes an object function in the visibility domain, as in Eq. (16). Most of the visibility data fall near the origin of the visibility plane, making more effective filtering of noise at low SNR levels. The standard deviation of δ with VP-OII is also lower than that with MIRA. These observations suggest that VP-OII is more resilient to noise than the conventional MIRA.

4.7. Effect of Channel Number

The effect of channel number and wavelength spacing is also analyzed by simulations with the configurations of GRAVITY and NPOI. Table 4 lists the performance with different channel numbers, at uniform wavelength spacing. The minimum and maximum wavelengths of GRAVITY are $\lambda_{\mathrm{G\,min}} = 1.97272\,\mu\mathrm{m}$ and $\lambda_{\mathrm{G\,max}} = 2.42727\,\mu\mathrm{m}$, respectively; and the minimum and maximum wavelengths of NPOI are $\lambda_{\mathrm{N\,min}} = 0.58177\,\mu\mathrm{m}$ and $\lambda_{\mathrm{N\,max}} = 0.84822\,\mu\mathrm{m}$, respectively. The number of recovered phases is larger when more channels are used. The phase errors, ϵ, are similar in these three cases. The rms pixel-wise difference is smaller when more channels are used with either VP-OII or MIRA. However, limited improvement (15.15 to 15.13) is observed by increasing the channel number from 11 to 16 in GRAVITY and from 9 to 16 in NPOI, because further increase of channel number no longer helps to extend the number of visibility data.

5. CONCLUSION

A VP-OII method is proposed to reconstruct an image by minimizing an object function in the visibility domain. A phase recovery technique is also proposed to extract additional information embedded in the closure-phase data. The initial guess is optimized first before modeling the visibility distribution of the image. The VP-OII method is sensitive to the initial guess, and the phase recovery technique can supply additional visibility data to optimize the initial guess. Compared with the conventional MIRA, the VP-OII method does not require any prior function, it requires only fewer tuning parameters, takes much shorter computational time and much less memory, and is more resilient to noise.

ACKNOWLEDGMENT

REFERENCES

1. Thureau, N. D., J. D. Monnier, W. A. Traub, R. Millan-Gabet, E. Pedretti, J. P. Berger, M. R. Garcia, F. P. Schloerb, and A. K. Tannirkulam, "Imaging the asymmetric dust shell around

CI Cam with long baseline optical interferometry," *Monthly Notices Roy. Astron. Soc.*, Vol. 398, No. 3, 1309–1316, 2009.

2. Renard, S., E. Thiebaut, and F. Malbet, "Image reconstruction in optical interferometry: Benchmarking the regularization," *Astron. Astrophys.*, Vol. 553, A64, Sep. 2011.

3. Thiébaut, E. and J. F. Giovannelli, "Image reconstruction in optical interferometry using a general framework to formally describe and compare different methods," *IEEE Signal Process. Mag.*, Vol. 27, No. 1, 97–109, Jan. 2010.

4. Hofmann, K. H. and G. Weigelt, "Iterative image reconstruction from the bisepctrum," *Astron. Astrophys.*, Vol. 278, 328–339, 1993.

5. Meimon, S. C., L. M. Mugnier, and G. Le Besnerais, "Reconstruction method for weak-phase optical interferometry," *Opt. Lett.*, Vol. 30, No. 14, 1809–1811, 2005.

6. Thiébaut, E., "MIRA: An effective imaging algorithm for optical interferometry," *SPIE Astron. Telescopes Instru.*, Vol. 7013, 70131I1-12, 2008.

7. Hofmann, K. H., G. Weigelt, and D. Schertl, "An image reconstruction method (IRBis) for optical/infrared interferometry," *Astron. Astrophys.*, Vol. 565, A48, 2014.

8. Ireland, M. J., J. D. Monnier, and N. Thureau, "Monte-Carlo imaging for optical interferometry," *Proc. SPIE*, 6268, 62681T, 2006.

9. Le Besnerais, G., S. Lacour, L. M. Mugnier, E. Thiebaut, G. Perrin, and S. Meimon, "Advanced imaging methods for long-baseline optical interferometry," *IEEE J. Select. Topics Signal Process.*, Vol. 2, No. 5, 767–780, Oct. 2008.

10. Le Bouquin, J. B., J. P. Berger, B. Lazareff, G. Zins, P. Haguenauer, et al., "PIONIER: A 4-telescope visitor instrument at VLTI," *Astron. Astrophys.* Vol. 535, A67, 2011.

11. Mourard, D., J. M. Clausse, A. Marcotto, K. Perraut, I. TallonBosc, et al., "VEGA: Visible spEctroGraph and polArimeter for the CHARA array: Principle and performance," *Astron. Astrophys.*, Vol. 508, 1073–1083, 2009.

12. Gillessen, S., F. Eisenhauer, and G. Perrin, "GRAVITY: A four-telescope beam combiner instrument for the VLTI," *SPIE Astron. Telescopes Instru.*, Vol. 7734, 77340Y-20, 2010.

13. Schutz, A., A. Ferrari, D. Mary, F. Soulez, E. Thiébaut, and M. Vannier, "PAINTER: a spatiospectral image reconstruction algorithm for optical interferometry," *J. Opt. Soc. Am. A*, Vol. 31, No. 11, 2334–2345, 2014.

14. Thiébaut, E., F. Soulez, and L. Denis, "Exploiting spatial sparsity for multiwavelength imaging in optical interferometry," *J. Opt. Soc. Am. A*, Vol. 30, No. 2, 160–170, Feb. 2013.

15. Auria, A., R. Carrillo, J. P. Thiran, and Y. Wiaux, "Tensor optimization for optical-interferometric imaging," *Monthly Notices Roy. Astron. Soc.*, Vol. 437, No. 3, 2083–2091, 2014.

16. Jankov, S., "Astronomical optical interferometry, I: Methods and instrumentation," *Serbian Astronom. J.*, No. 181, 1–17, 2010.

17. Lawson, P. R., W. D. Cotton, C. A. Hummel, J. D. Monnier, et al., "The 2004 optical/IR interferometry imaging beauty contest," *Proc. SPIE*, Vol. 5491, 886–899, 2004.

18. Armstrong, J. T., D. J. Hutter, E. K. Baines, J. A. Benson, R. M. Bevilacqua, T. Buschmann, J. H. Clark, III, A. Ghasempour, J. C. Hall, R. B. Hindsley, et al., "The Navy Precision Optical Interferometer (NPOI): An update," *J. Astron. Instru.*, Vol. 2, No. 2, 1340002, 2013.

19. Le Bouquin, J. B., S. Lacour, S. Renard, E. Thiébaut, A. Merand, and T. Verhoelst, "Pre-maximum spectro-imaging of the Mira star T Lep with AMBER/VLTI," *Astron. Astrophys.*, Vol. 496, L1, Apr. 2009.

20. Bourguignon, S., D. Mary, and E. Slezak, "Restoration of astrophysical spectra with sparsity constraints: Models and algorithms," *IEEE J. Select. Topics Signal Process.*, Vol. 5, No. 5, 1002–1013, Sep. 2011.

21. Baron, F., W. D. Cotton, P. R. Lawson, S. T. Ridgway, A. Aarnio, et al., "The 2012 interferometric imaging beauty contest," *Proc. SPIE*, Vol. 8445, 1E1-14, 2012.

22. Pauls, T. A., J. S. Young, W. D. Cotton, and J. D. Monnier, "A data exchange standard for optical (visible/IR) interferometry," *Pub. Astron. Soc. Pacific*, Vol. 117, No. 837, 1255–1262, Nov. 2005.